UCSF
UC San Francisco Previously Published Works

Title

Parceling Human Accumbens into Putative Core and Shell Dissociates Encoding of Values for Reward and Pain

Permalink

https://escholarship.org/uc/item/3xk66408

Journal

Journal of Neuroscience, 33(41)

ISSN

0270-6474

Authors

Baliki, Marwan N
Mansour, Ali
Baria, Alex T
et al.

Publication Date

2013-10-09

DOI

10.1523/jneurosci.1731-13.2013

Peer reviewed

Systems/Circuits

Parceling Human Accumbens into Putative Core and Shell Dissociates Encoding of Values for Reward and Pain

Marwan N. Baliki,[1]* **Ali Mansour,**[1]* **Alex T. Baria,**[1] **Lejian Huang,**[1] **Sara E. Berger,**[1] **Howard L. Fields,**[2] and **A. Vania Apkarian**[1]

[1]Department of Physiology, Northwestern University Feinberg School of Medicine, Chicago, Illinois 60611, and [2]Department of Neurology and Ernest Gallo Clinic & Research Center, University of California, San Francisco, Emeryville, California 94608

In addition to their well-established role in signaling rewarding outcomes and reward-predictive cues and in mediating positive reinforcement, there is growing evidence that nucleus accumbens (NAc) neurons also signal aversive events and cues that predict them. Here we use diffusion tractography to subdivide the right NAc into lateral–rostral (putative core, pcore) and medial–caudal (putative shell, pshell) subdivisions in humans. The two subregions exhibited differential structural connectivity, based on probabilistic tractography, to prefrontal cortical and subcortical limbic regions. We also demonstrate unique roles for each of the two subdivisions for monetary reward and thermal pain perception tasks: pshell signaling impending pain and value predictions for monetary gambles and pcore activating with anticipation of cessation of thermal pain (signaling reward value of analgesia). We examined functional connectivity for resting state, monetary reward, and thermal pain tasks, and for all three conditions observed that pcore and pshell of right NAc exhibit distinct patterns of synchrony (functional connectivity) to prefrontal cortical and subcortical limbic targets within the right hemisphere. To validate the NAc segregation, we mirrored the coordinates of right NAc pcore and pshell onto the left hemisphere and examined structural and resting state connectivity in the left hemisphere. This latter analysis closely replicated target-specific connections we obtained for the right hemisphere. Overall, we demonstrate that the human NAc can be parceled based on structural and functional connectivity, and that activity in these subdivisions differentially encodes values for expected pain relief and for expected monetary reward.

Introduction

The ability to predict favorable and aversive outcomes from environmental cues is critical to optimal action selection. Ample evidence now points to the fundamental role of the mesolimbic circuitry, including nucleus accumbens (NAc), in encoding value for rewarding and aversive stimuli and in determining the corresponding behavioral outcome. Yet, the neural circuits underlying these functions in humans are incompletely described. Identifying the circuits is critical for understanding how punishment, positive reinforcement, and their predictive cues contribute to behaviors and how learning contributes to common clinical disorders, such as drug addiction and chronic pain.

Electrophysiological studies have shown that midbrain dopaminergic neurons encode reward prediction error and contribute to approach behaviors elicited by reward predictive cues (Schultz et al., 1997; Montague and Berns, 2002; Fields et al., 2007), and behavioral studies indicate the participation of mesocorticolim-

bic circuitry in appetitive behaviors reinforced by conditioned cues (Schultz et al., 1997; Montague and Berns, 2002; Fields et al., 2007). Consistently, human imaging studies show the mesocorticolimbic system participates in decision making under uncertainty across diverse domains, such as palatable food, sex, drugs, monetary, and other rewards, or reward predictive cues (Zahm, 2000; Ambroggi et al., 2008; Basar et al., 2010). A growing body of evidence has expanded this traditional view from a monovalent pathway signaling reward by demonstrating that it also signals actual and impending aversive events (O'Doherty, 2004; Montague et al., 2006; Platt and Huettel, 2008). Animal electrophysiology (Mirenowicz and Schultz, 1996; Joshua et al., 2008; Brischoux et al., 2009) and human brain imaging provide evidence for activation of components of mesocorticolimbic circuitry in response to pain, pain predictive cues, and reward value of pain relief (Becerra et al., 2001; Bassareo et al., 2002; Seymour et al., 2005, 2007; Scott et al., 2006; Becerra and Borsook, 2008; Roitman et al., 2008; Baliki et al., 2010; Wanigasekera et al., 2012).

Despite these advances, the specificity to which the NAc differentially responds to positive and negative cues remains unclear. Yet, theoretical considerations and experimental outcomes suggest that positive and negative stimuli may be processed separately (Cacioppo, 1994): (1) multiplicity of control systems between NAc and ventral pallidum that reiteratively link separate circuits (Alexander et al., 1986; Zahm and Brog, 1992; Thompson and Swanson, 2010; Lüscher and Malenka, 2011); (2) neurochemical modulation that differs for hedonic and motivational

functions (Baldo and Kelley, 2007; Hikida et al., 2010, 2013); (3) differential neural representations of salience and reward in the rodent NAc (Smith et al., 2011), and in specific VTA neurons in the primate (Bromberg-Martin et al., 2010; Cohen et al., 2012). Therefore, given that NAc has two anatomically distinct subregions, the shell and core, we hypothesize that subregions of NAc in the human differentially encode rewarding and aversive environmental cues. As subdivisions of NAc have not been delineated in human brain imaging studies, neither structural nor functional connections, nor possible functional specializations of the NAc subdivisions, are understood in humans. We address these issues in the current study.

Materials and Methods

Subjects. Twenty-six healthy subjects (14 males, 12 females; average age: mean, 38.11 years; SEM, 1.62 years; range, 27–53 years) participated in the study, in which diffusion-weighted (DTI), T1-weighted, and resting state functional images were collected. Of the 26 subjects, 15 subjects also participated in the gambling experiment, which was conducted in a separate session. All participants were right-handed and had no history of neurological or psychiatric impairment. Subjects gave informed consent to procedures approved by Northwestern University Institutional Review Board committee. In addition, we present data from a previously published study (Baliki et al., 2010) where we scanned 16 healthy controls (8 males, 8 females; average age: mean, 38.77 years; SEM, 2.76 years; range, 23–59 years) during a thermal pain rating task.

Imaging data acquisition. All data were acquired with a 3 T Siemens Trio whole-body scanner with echo-planar imaging capability using the standard eight-channel radiofrequency head coil. DTI data were acquired using echo planar imaging (72×2-mm-thick axial slices; matrix size, 128×128; field of view, 256×256 mm^2, giving a voxel size of $2 \times 2 \times 2$ mm). Images had an isotropic distribution along 60 directions using a b value of $1000 \, \text{s} \cdot \text{mm}^{-2}$. For each set of diffusion-weighted data, eight volumes with no diffusion weighting were acquired at equidistant points throughout the acquisition. The total scan time for the diffusion-weighted imaging protocol was ~11 min. Functional resting state scans (244 volumes, 10 min) were acquired for 26 subjects. Participants were instructed to stay alert and keep their eyes open for the duration of the scan. Images were obtained with the following parameters: Multislice T2*-weighted echo-planar images with repetition time (TR) = 2.5 s, echo time (TE) = 30 ms, flip angle = 90°, FOV = 256 mm, slice thickness = 3 mm, and in-plane resolution = 64×64. The 40 slices covered the whole brain from the cerebellum to the vertex. Gambling task functional scans were collected with the following parameters: multislice T2*-weighted echo-planar images with TR = 2.5 s, TE = 30 ms, flip angle = 90°, FOV = 256 mm, slice thickness = 3 mm, in-plane resolution = 86×72. The 40 slices covered the whole brain from the cerebellum to the vertex. Each subject underwent two consecutive scans of 281 volumes each (~12 min). Thermal pain rating functional scans are described in a previous report (Baliki et al., 2010) and had the following parameters: T2*-weighted echo-planar images were obtained with the following parameters: repetition time TR = 2.5 s, echo time TE = 30 ms, flip angle = 90°, slice thickness = 3 mm, in-plane resolution = 64×64. The 36 slices covered the whole brain from the cerebellum to the vertex. Also, for all participants, MPRAGE type T1-anatomical brain images were acquired using the following parameters: voxel size $1 \times 1 \times 1$ mm, TR = 2500 ms, TE = 3.36 ms, flip angle = 90°, in-plane matrix resolution 256×256, 160 slices, field of view 256 mm.

DTI connectivity-based parcellation of NAc. The DTI connectivity-based parcellation was performed using procedures described in a previous report (Tomassini et al., 2007). For each subject, T1-weighted scans were processed using FIRST (fMRIB Integrated Registration and Segmentation Tool) for subcortical brain segmentation using Bayesian shape and appearance models to localize each subject's NAc. Based on learned models, FIRST searches through linear combinations of shape modes of variation for the most probable shape instance given the observed intensities in the T1 image (Tomassini et al., 2007). Subject-specific NAc maps were linearly registered to standard space, based on

transformations optimized for subcortical structures. These ROIs were then overlaid, creating a group-average representative NAc ROI.

FAST (fMRIB Automated Segmentation Tool) was used to segment the 3D T1 images of the brain into different tissue types (gray matter, white matter, and CSF) while also correcting for spatial intensity variations. The underlying method is based on a hidden Markov random field model and an associated Expectation-Maximization algorithm, yielding probabilistic and/or partial maps. For each subject, we transformed the gray matter mask into standard space using FSL linear registration tool (FLIRT), which defined target voxels.

For all seed voxels, whole-brain probabilistic tractography was run using PROBTRACKX. A total of 5000 samples were drawn to build the a posteriori distribution of the connectivity distribution. The connection probability between an NAc seed voxel and any target voxel in the brain is defined as the sum of sample fiber lengths connecting these two voxels. For each subject, the result was connection probabilities for all seed voxels with the number of target voxels.

The connectivity matrix, A, between NAc seed voxels and target voxels was derived, as described previously (Tomassini et al., 2007) and used to generate a symmetric cross-correlation matrix, of dimensions number of seeds $\times$ number of seeds. The rows in the matrix were permuted using k-means clustering, repeated 10 times, to define two regions. The goal of clustering the cross-correlation matrix is to group together regions that share a similar connectivity profile with the rest of the brain. Because it is more likely for NAc voxels that share a spatial proximity to share similar connectivity profiles, we included a distance constraint, by adding a (scaled) Euclidean distance matrix to the cross-correlation matrix. The resulting clusters were then constrained to consist of voxels that are spatially contiguous, although the border between clusters is still guided by remote connectivity information.

The automated classification using k-means clustering produced individual parcellation of the NAc into subdivisions as groups of elements that were strongly correlated with each other and weakly correlated with the rest of the matrix. Results from clustering are mapped back onto the brain. Group-level subdivisions were determined by overlapping all subjects' subdivisions, then determining the regions of 80% overlap. The group-averaged two subdivisions were then used as ROIs to define both diffusion and functional connection fingerprints.

fMRI data preprocessing. Data were processed using FSL software. The first four volumes from each functional dataset were removed. Functional datasets were then preprocessed using rigid-body motion correction, slice scans timing correction, linear trend removal, skull extraction using BET, and high-pass temporal filtering (150 s). We did not apply any spatial smoothing, to avoid blurring differences in connectivity patterns between neighboring voxels. After preprocessing, several sources of noise, which may contribute to non-neuronal fluctuations, were removed through linear regression. These included the six parameters obtained by rigid body correction of head motion and head rotation, the global BOLD signal averaged over all voxels of the brain, white matter signal, and ventricular signal.

Gambling task procedure and stimuli. Fifteen healthy subjects participated in this task, which was adapted from a published report (Tom et al., 2007). Subjects were given $30 in cash at a date before testing and told that it was theirs to keep, but some of this may be going toward the future gambling task. Before scanning, all subjects were trained on the task. During the scanning session, stimuli were presented using Presentation software, version 14. Trials began with a red dot (2.5 s) followed by a display showing the amount of potential gain (in green) and amount of potential loss (in red). Subjects then had 5 s (decision interval) to consider their choice before a green dot signaled for an "accept" or "reject" response, made with a computer mouse. Value amounts ranged from $10 to $38, with increments of $4 for gains, and $5 to $19, with increments of $2 for losses. Intertrial intervals were randomized and lasted 10–12.5 s. Each potential gain/loss combination was presented over a course of 64 trials, with 32 trials per scan. Subjects' choices had real monetary consequences to best emulate real-world decision-making. At the end of the test day, one trial was randomly selected and subjects were paid in cash according to their choice on that trial. Thus, individuals had a 50/50 chance for gaining or losing money.

For each participant, the data were fit with a straight line using the size of each potential gain and loss as independent variables, and the participant's acceptance/rejection as the dependent variable as described in a previous report (Tom et al., 2007). The resulting regression coefficients for loss and gain variables served as individual measures of sensitivity. The ratio of loss-to-gain responses was then used to calculate each participant's level of behavioral loss aversion (λ). All fits, regression coefficients, and λ values were calculated using MATLAB version R2010b (MathWorks).

Thermal pain rating task procedures and stimuli. The thermal pain rating task was described previously in detail (Baliki et al., 2010). In brief, subjects were scanned while rating their pain in response to thermal stimuli applied to their lower back just off midline. All subjects underwent an initial training phase before scanning, in which they learned to use the finger-span device, comprised of a potentiometer the voltage of which was digitized and time-stamped in reference to fMRI image acquisition and connected to a computer providing visual feedback of the ratings. A purpose-built, fMRI-compatible thermal stimulator delivered fast-ramping (20°C per second), painful, thermal stimuli (baseline 38°C, peak temperatures 47°C, 49°C, and 51°C) via a contact probe (1×1.5 cm peltier). Durations and intensities of thermal stimuli as well as interstimulus intervals were presented in a pseudorandom fashion. During the functional imaging session, 9 noxious thermal stimuli ranging in duration from 12 to 30 s were used.

Intrinsic brain connectivity analysis. After preprocessing the fMRI data, we performed functional connectivity analysis using the two group-averaged NAc subdivisions as seeds. Whole-brain voxelwise regression was performed for each subject using general linear modeling. The BOLD signal averaged over each cluster was used to generate parametric estimate (PE) maps for each individual and condition (pshell and pcore). PE maps for the pcore and pshell were generated for the resting state, gambling task, and thermal pain rating task. Differences in brain connectivity between pcore and pshell were performed using an ROI analysis.

NAc functional and anatomical fingerprints. Anatomical fingerprints for the determined right NAc subdivisions (pcore and pshell) were generated closely following previously described methods (Tomassini et al., 2007). We first performed whole-brain probabilistic tractography for the NAc subdivisions in each individual. We then evaluated the connectivity from the right NAc subdivisions to ipsilateral cortical and subcortical ROIs. Target ROIs were defined from the Harvard-Juliet atlas and included subcallosal cortex (SCC), frontal pole (FP), hippocampus (HIP), amygdala (AMYG), basal ganglia (BG), thalamus (TH), cingulate gyrus (CG), insula (INS), paracingulate gyrus (PCG), and orbital frontal cortex (OFC). For each subject, the total probability of connection between the seed region (pcore or pshell) and each target region was computed separately for each subdivision of NAc and then normalized by dividing by the total sum of probability to any gray matter voxel in the ipsilateral hemisphere, so that these values represent connection probability as a percentage of total connections in the hemisphere. Any target mask with a normalized connectivity probability that was <0.2% of all hemispheric probability was excluded from additional analyses. Connection probabilities of those regions, which survived thresholding, were divided by the size of the target region, to produce connection probabilities adjusted for the volume of the target region. These normalized values were then used to generate structural connectivity fingerprints. Differences in connectivity for each target to the NAc subdivisions were computed using a two-way repeated-measures ANOVA. Given that the right NAc subdivisions are based on maximally uncorrelated DTI connectivity profiles, the target-based analysis in the right hemisphere can be considered *post hoc*, intending to unravel structures that differentially are connected to each subdivision of NAc. To validate the results, we transformed the right NAc coordinates to the left brain and performed the target-based analysis of the left NAc subdivisions to left target regions (same list as above), where obtained results are considered unbiased.

Similarly functional fingerprints were generated using the PE values from the connectivity analysis calculated separately for each subdivision of NAc. The mean PE for each target was computed by averaging all the PE values from voxels within the target ROI. As the functional connectivity is performed using independent scans from that of DTI, they too

are considered as unbiased estimates of differentiation of connectivity between NAc subdivisions, which was performed in left and right hemispheres. Differences in connectivity were determined using three-way ANOVA (NAc subdivisions, task types, and targets). *Post hoc* comparisons between pcore and pshell connectivity for each scan were determined using Tukey's test.

BOLD analysis. The NAc ROIs were reverse-normalized and projected back into the un-normalized individual brain space. The BOLD signal was determined by first averaging the raw data for all voxels across (and within) the ROI from the preprocessed functional data, which is corrected for head motion artifacts and non-neuronal signal. Percentage BOLD change was then computed as the deviation from the mean for voxels within the ROI. The BOLD time course during stimulation epochs (gambling or pain) was determined by triggered averaging across the stimulus repetitions and subjects, over a 40 s window where time = 0 was designated the beginning of task or stimulus. The gambling task ends within 20 s; thus, the BOLD responses displayed for this condition also reflect activity for previous and subsequent trials.

Results

DTI connectivity identifies two spatially discrete subdivisions of NAc

To subdivide the NAc into two portions, we first had to identify borders of right NAc. T1-weighted anatomical scans were used to segment NAc. Subject-specific NAc voxels were transformed into standard space and overlapped across all subjects to generate a unified NAc ROI in standard space. The group NAc ROI consisted of 94 voxels ($2 \times 2 \times 2$ mm) that were represented across all subjects.

We then used DTI data in the same subjects to cluster the NAc connectivity patterns into two components. For each NAc voxel in every subject, whole-brain probabilistic tractography was performed to determine the extent of structural connectivity to each gray matter voxel in the brain based on local probability density functions. We then used DTI connectivity-based parcellation to subdivide the standard right NAc into two portions, based on clustering the covariance of whole-brain structural connectivity. Individual parcellation and covariance clusters (with and without a distance constraint) for all subjects are shown in Figure 1. In each subject, we observe an approximate medial–lateral parcellation, dividing the NAc into two approximately equal parts. Parcellations were based on the covariance incorporating distance. Yet, the results differ minimally when this constraint is not included.

Group-level subdivisions of right NAc were determined as regions of 80% overlap across individual subjects' parcellation of NAc, resulting in discrete, spatially contiguous subdivisions, with no overlap (Fig. 2A,B). The first cluster exhibited a medial–caudal representation (43 voxels), whereas the second cluster showed a lateral–rostral representation (51 voxels). The location and shape of the two clusters approximately matched cytoarchitecturally identified NAc core and shell in postmortem human tissue (Fig. 2C,D). Based on this correspondence, we define the medial–caudal portion as putative shell (pshell) and the lateral–rostral portion as putative core (pcore) of NAc. These masks are available upon request.

NAc subdivisions possess distinct structural connections

The two subdivisions that we identify for right NAc are based on whole-brain structural connectivity differences. Yet, we do not know specific brain regions that differentially link to pcore and pshell. Tracer-based studies in rat and monkey show that multiple frontal cortical and subcortical limbic regions establish distinct connections with subdivisions of NAc (Meredith et al.,
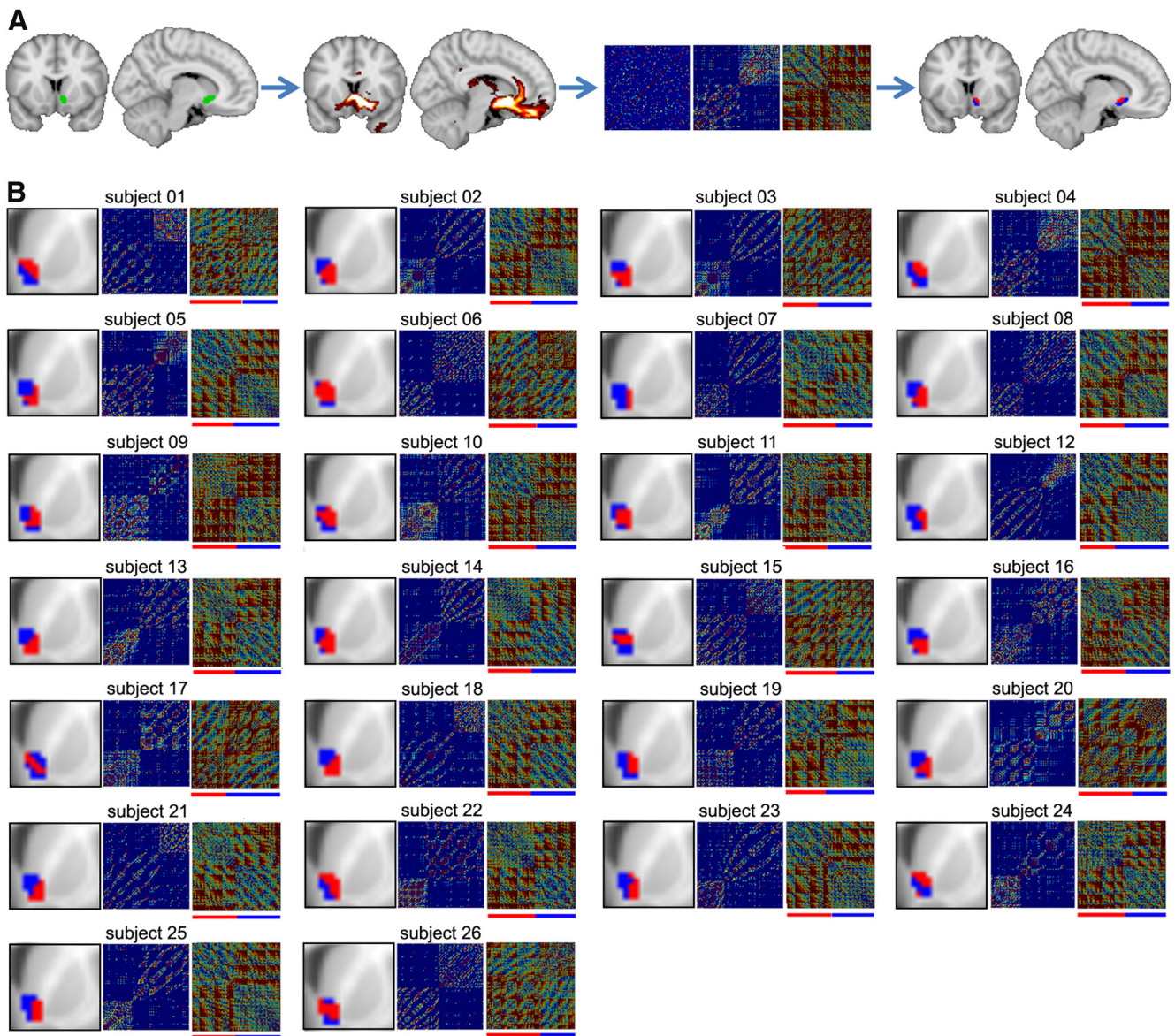
A

B

Figure 1. DTI tractography parcellation identifies two distinct subdivisions in the right NAc in individual subjects. ***A***, Summary of the steps leading to the NAc clustering in an example subject. Left brain images, NAc region (green) and resulting tracks (red). Middle panels, Cross-correlation matrices indicating the degree of similarity in connectivity pattern between the NAc voxels. Leftmost matrix, Cross-correlation from all NAc voxels. Middle, Matrix reorganized based on the *k*-means cluster algorithms. Rightmost panel, Matrix normalized by distance. This final matrix was used to delineate the two different clusters indicated by red and blue bars beneath the matrix. Right brain images, Two resulting clusters (blue and red) projected back on the brain. ***B***, Results of the connectivity-based clustering for all 26 subjects. For each subject: left panel, part of coronal slice at $y = 12$ mm and the corresponding NAc clusters; middle and right panels, reorganized and normalized cross-correlation matrices, respectively.

1996; Fudge and Haber, 2002; Haber and Knutson, 2010; Haber, 2011). Based on these animal results, we chose 10 targets of interest (Fig. 3*A*) and calculated seed-to-target structural connectivity probabilities for the two subdivisions of right NAc. The group-averaged white matter tracts identified for each part of NAc identified relatively distinct pathways (Fig. 3*B*). The connection probabilities for the 10 regions were normalized for the volume of the individual target and contrasted using a two-way repeated-measure ANOVA (NAc subdivisions and target regions). DTI connectivity exhibited significant target effect ($F_{(9,250)} = 46.46$, $p < 0.0001$) and subdivision × target interaction ($F_{(9,250)} = 14.83$, $p < 0.0001$), but a nonsignificant subdivision effect ($F_{(1,250)} = 2.01, p = 0.16$). Significant differences in the *p*core and *p*shell connectivity to each target regions were determined using a Tukey-HSD *post hoc* analysis. The *p*core exhibited higher struc-

tural connectivity to right BG, FP, and OFC. In contrast, the *p*shell showed higher connectivity to right AMYG. Both right NAc subdivisions showed similar strength connectivity to right TH, CG, HIP, INS, PCG, and SC (Table 1). Thus, these DTI-based seed-to-target and white matter track differences imply that *p*shell and *p*core are comprised of relatively distinct structural circuitry.

NAc subdivisions show differential responses during a monetary gambling task

Human neuroimaging studies have consistently implicated NAc in signaling monetary gains or losses. Here we investigate differential responses of the right NAc subdivisions in a monetary gambling task. We collected fMRI data while participants decided whether to accept or reject mixed gambles that
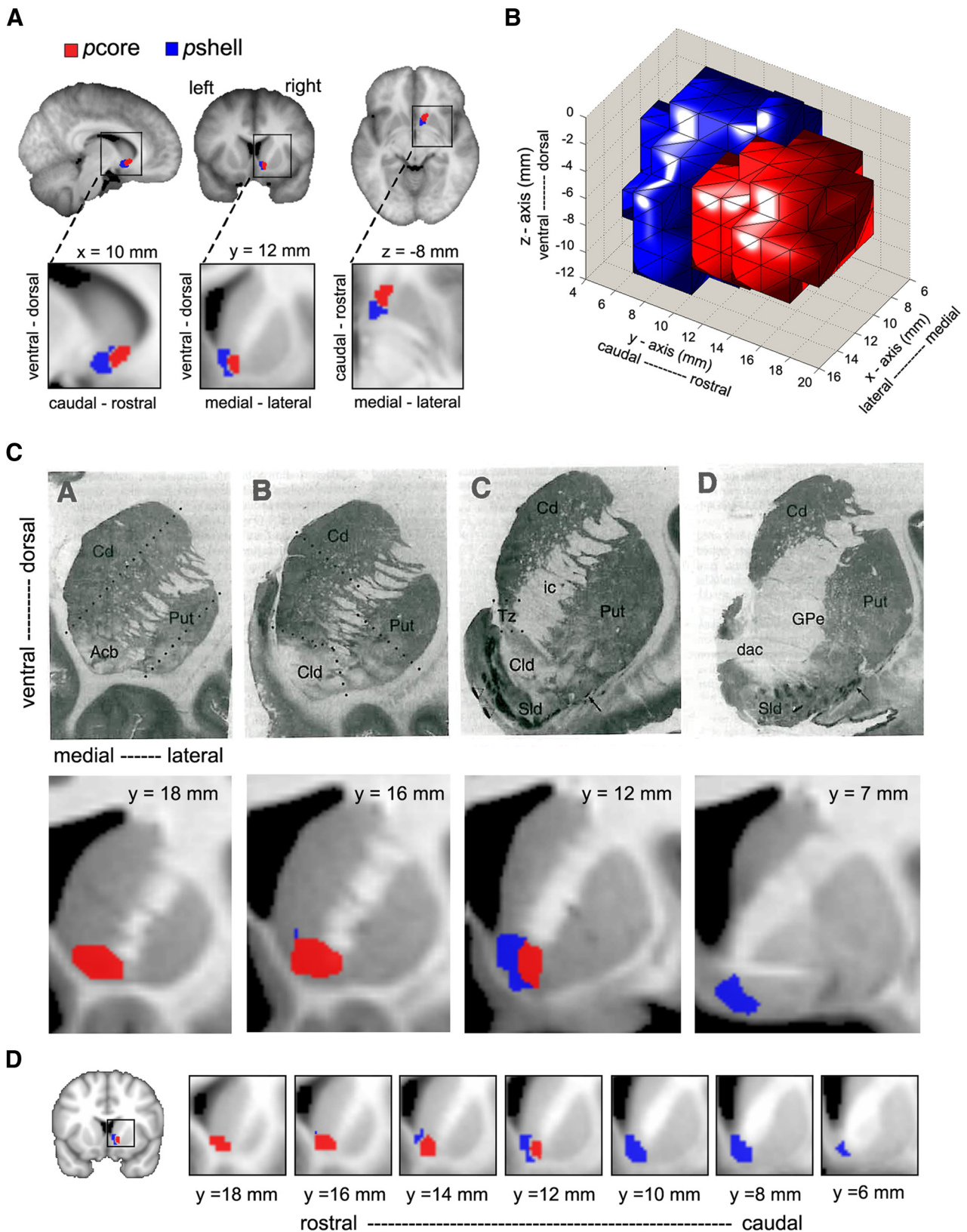
Figure 2. The human NAc can be divided into two subdivisions. **A**, Group-averaged DTI-based clustering of the right NAc into a medial–caudal (blue, putative shell, pshell) and a lateral–rostral (red, putative core, pcore) subdivision. Group-averaged clusters were determined as regions showing 80% overlap across individual subjects ($n = 27$). **B**, Three-dimensional rendering of pcore and pshell, observed from a right, lateral view. **C**, Top row represents a series of coronal sections through the striatum from a single human brain, illustrating the DAMGO binding at four rostrocaudal levels. Images taken from Voorn et al. (1996), in which they identify the accumbens (Acb), its Core-like division (Cld), and shell-like division (Sld). The two most rostral slices (**A**, **B**) contain only Cld, delineated by broken lines in B, whereas **D** identifies only Sld. Bottom row, Group average DTI-based parcellation of the NAc into the pcore and pshell. The pcore (red) and pshell (blue) subdivisions approximate Cld and Sld, respectively. **D**, Detailed rostrocaudal coronal slices of group-averaged clustering of the human NAc (higher values correspond to rostral slices and lower values to caudal slices).
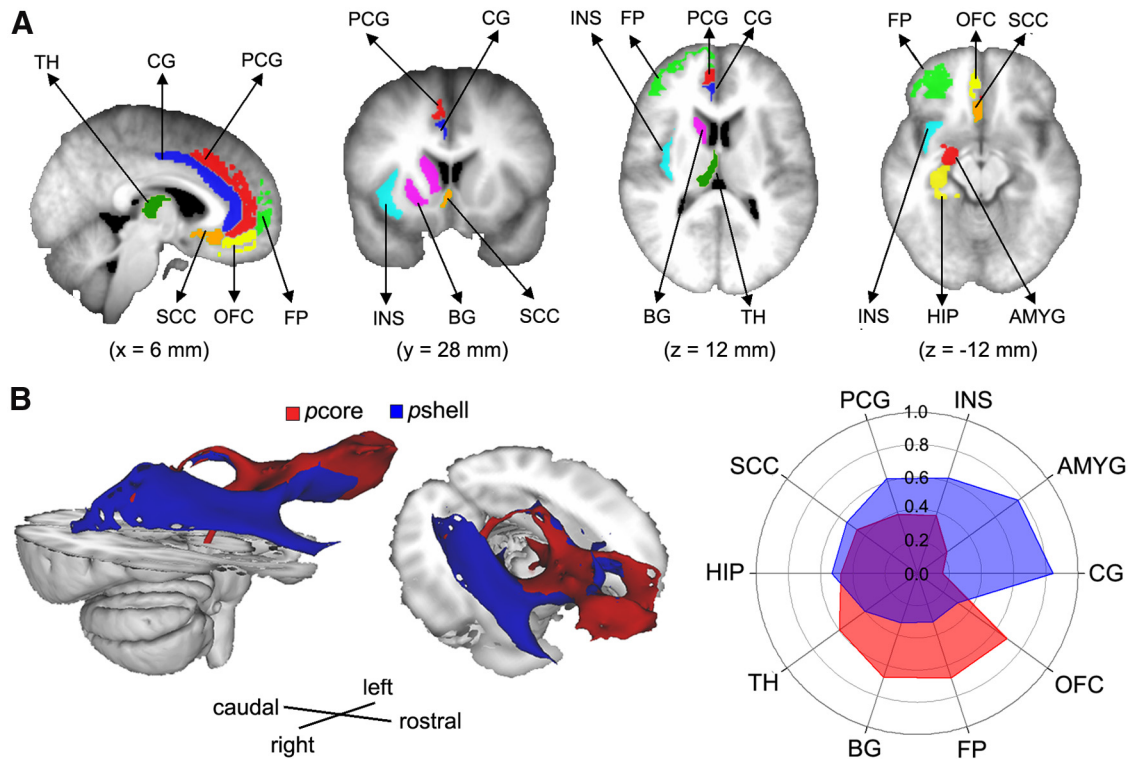
Figure 3. The NAc subdivisions exhibit distinct structural connectivity patterns. **A**, Brain slices showing the cortical and subcortical targets of interest, which included the TH, BG, CG, PCG, HIP, AMYG, INS, SCC, OFC, and FP. The targets were all identified from the Harvard-Oxford cortical and subcortical structural atlas and were restricted to gray matter within the right hemisphere. **B**, Brain images show the group average white matter tracts for the *p*core (red) and *p*shell (blue) in the right hemisphere. Polar plot represents the structural connectivity fingerprints in the right hemisphere from right NAc subdivisions. The values indicate relative connection probabilities of white matter tracks, based on DTI tractography for *p*shell and *p*core to the targets.

Table 1. Normalized structural (DTI) connectivity based differences between the two subdivisions of NAc[a]

ROI	NAc *p*core	NAc *p*shell	*p*core > *p*shell (*p*)	Target size (ml)
AMYG	0.55 ± 0.10	1.87 ± 0.26	<0.0001	1.53 ± 0.08
BG	2.65 ± 0.22	1.27 ± 0.15	<0.0001	4.37 ± 0.25
CG	0.05 ± 0.08	0.22 ± 0.38	NS	0.97 ± 0.18
FP	0.97 ± 0.20	0.45 ± 0.09	<0.05	8.23 ± 1.63
HIP	0.25 ± 0.04	0.28 ± 0.06	NS	3.33 ± 0.23
INS	0.02 ± 0.03	0.07 ± 0.01	NS	0.84 ± 0.13
OFC	1.34 ± 0.30	0.61 ± 0.18	<0.05	1.96 ± 0.09
PCG	0.06 ± 0.03	0.09 ± 0.02	NS	1.70 ± 0.26
SCC	2.95 ± 0.40	3.45 ± 0.29	NS	1.55 ± 0.11
TH	0.93 ± 0.15	0.62 ± 0.10	NS	3.77 ± 0.10

[a]Data are mean ± SEM; percentage structural connection strength between seed regions (*p*core and *p*shell) and 10 target regions. Each value is divided by the sum of connections to all the targets, so as to be expressed as a percentage of the total connections to all the targets, which is then normalized by dividing the respective individual target volume. Statistical contrasts for two-way ANOVA *post hoc* analysis are indicated.

NS, Not significant.

offered a 50/50 chance of gaining or losing money (Fig. 4A). We first assessed behavioral sensitivity to gains and losses (loss aversion) by fitting a logistic regression to each participant's acceptability judgments, using the size of the gain and loss as independent variables (Tom et al., 2007). Subjects showed an average loss aversion of 1.89 (SEM, 0.45; range, 0.92–7.33), that closely matched the results of the original study (Tom et al., 2007). These results indicate that participants, on average, are indifferent to gambles where potential gain was twice the amount of the potential loss (Fig. 4B).

We then examined whether the right NAc subdivisions showed distinct activation patterns during accept and reject choices. Group-averaged time courses of the BOLD signal for *p*core and *p*shell during the accept and reject trials are displayed in Figure 4C. The BOLD signal in right NAc *p*core increased similarly for both accepted (mean ± SEM %BOLD change was 0.23 ± 0.08) and rejected (mean ± SEM %BOLD change was 0.25 ± 0.08) choices (two-tailed paired *t* test: $t = -0.14$, $p = 0.85$). In contrast, the BOLD signal in the right NAc *p*shell exhibits differential responses for the accept and reject choices. The NAc *p*shell showed increased activity in response to the accepted choices (mean ± SEM %BOLD change was 0.14 ± 0.11) and decreased activity to the rejected choices (mean ± SEM %BOLD change was −0.11 ± 0.12). Furthermore, percentage BOLD changes during the accept and reject choices were significantly different (two-tailed paired *t* test: $t = 3.14$, $p < 0.01$). To investigate the association between the right *p*core and *p*shell activity and behavior, we computed the percentage BOLD response for each subdivision across all 16 cells in the group average potential gain/loss matrix (Fig. 4D). Whereas the *p*core did not exhibit any differential activation, the *p*shell reflected decision values. The relationship between behavior outcome (probability of acceptance) and BOLD responses in the *p*core and *p*shell was computed using a linear correlation across all 16 cells in the group average potential gain/loss matrix. The probability of acceptance exhibited a significant correlation with the percentage BOLD change in *p*shell ($r = 0.96$, $p < 0.001$), but not in the *p*core ($r = 0.11$, $p = 0.92$). Therefore, for monetary gambles, the NAc *p*core appears to be similarly activated for both accepted and rejected choices trials, whereas the NAc *p*shell signals reward (appetitive) prediction.
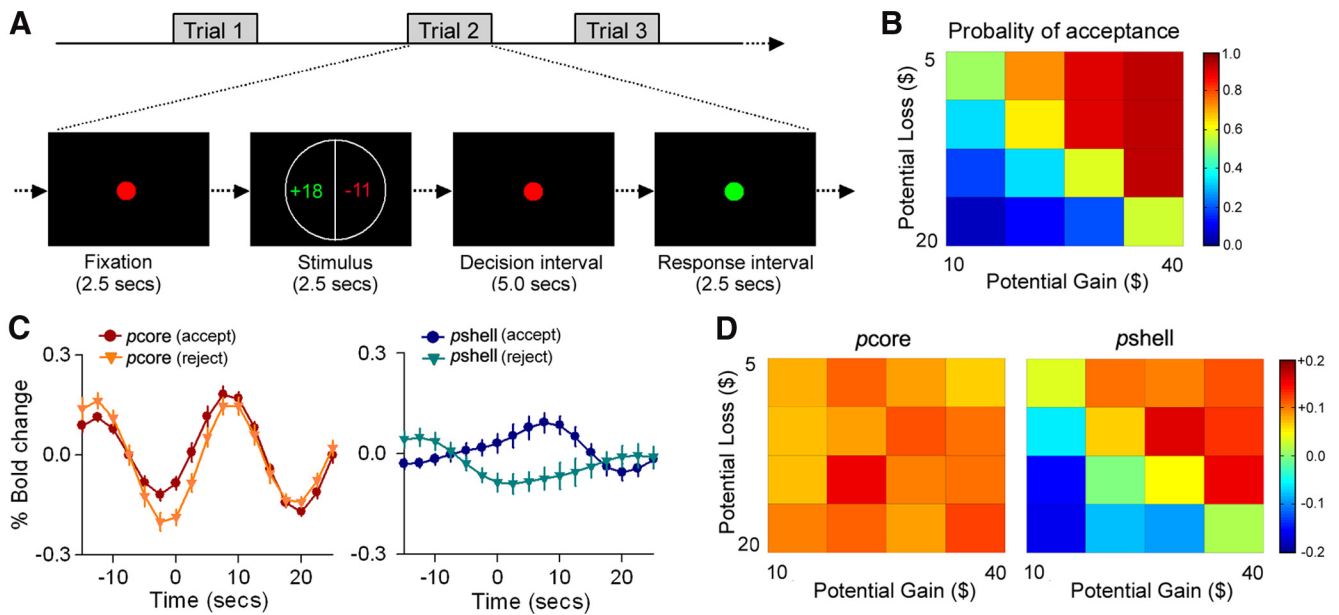
Figure 4. The NAc subdivisions exhibit specific activity during a monetary gambling task. **A**, The monetary gambling task design, derived from Tom et al. (2007). During each trial, a display showing the size of the potential gain (in green) and loss (in red) was presented for 2.5 s. This was followed by a 5 s decision interval and a 2.5 s response interval. After an accept or reject response, a variable interval was presented (10 – 15 s) to allow for adequate deconvolution of fMRI responses. **B**, Color-coded heatmap matrix of group-averaged probability of gamble acceptance at each level of accept/reject: red represents high willingness to accept the gamble; blue represents low willingness to accept the gamble. **C**, Group average time course of BOLD responses (% change from baseline), for the *p*core and *p*shell of right NAc, during accepted and rejected trials. The *p*core showed similarly increased responses for both accepted and rejected choices, whereas the *p*shell showed differential increased responses for acceptances and decreased responses for rejections. **D**, Heatmaps were created by averaging %BOLD change versus baseline BOLD, within the *p*core and *p*shell of right NAc, for each of the 16 cells in the potential gain/loss matrix; color coding reflects the strength of neural response for each condition: dark red represents the strongest activation; dark blue represents the strongest deactivation. The *p*core did not exhibit any differential activation, whereas the *p*shell reflected decision values.

NAc subdivisions differentially encode onset and offset of pain

We previously showed that, for painful thermal stimuli applied to the skin, the NAc BOLD signal reflects both the salience for painful stimulus onset and analgesia reward at stimulus offset (Baliki et al., 2010, their Fig. 2, labeled p1 and p2, respectively). Here we reexamine these data to test whether subdivisions of right NAc distinguish the two pain-related predictions.

When the BOLD signal was extracted separately for the *p*core and *p*shell of right NAc, we observed that the *p*shell response was transiently positive at thermal pain onset (mean ± SEM %BOLD at p1 for *p*shell compared with baseline was 0.28 ± 0.05, and for *p*core was 0.03 ± 0.04; two-tailed paired t test: $t = 7.13, p < 0.01$), whereas the NAc *p*core response was transiently positive at pain offset (mean ± SEM %BOLD at p2 for *p*core compared with baseline was 0.26 ± 0.06, and for *p*shell was −0.05 ± 0.05; two-tailed paired t test: $t = 6.88, p < 0.01$) (Fig. 5). Moreover, we observe that *p*shell response was not related to the experienced pain whereas the *p*core response was (correlation, r, between peak BOLD and maximum pain rating at p1 for *p*shell was $r = 0.08, p > 0.7$, whereas at p2 for *p*core $r = 0.78, p < 0.01$). The shape, peak, and temporal evolution of these responses match our previous findings for the entire NAc (Baliki et al., 2010), where we also showed that the NAc responses follow the derivative of the thermal stimulus, thereby corresponding to prediction errors. Moreover, we showed that the NAc signal at stimulus onset was invariant, whereas at stimulus offset, it was proportional to the pain experienced by the subjects. Thus, the previous results, coupled with the current observations, imply that the NAc *p*shell response reflects a prediction/anticipation or salience signal, and the NAc *p*core response is a valuation response (reward predictive signal) that signals the negative reinforcement value of cessation of pain (i.e., anticipated analgesia).

NAc subdivisions possess distinct functional connectivity

Given the structural and functional specificity of the two subdivisions of right NAc, we investigated their functional connectivity during resting state, thermal pain rating, and gambling task scans. The average BOLD signals from the two subdivisions of right NAc were used to perform a whole-brain general linear model analysis, yielding two functional connectivity maps for each subject and task. Differences in functional connectivity were assessed using an ROI analysis. The mean PE for the 10 ROIs (Fig. 3) was calculated and entered into a three-way ANOVA with NAc subdivisions (*p*core and *p*shell) and task (resting-state, gambling, and thermal pain) and the 10 target ROIs as predictors.

The functional connectivity fingerprints for *p*core and *p*shell for all tasks are displayed in Figure 6 for right NAc. Overall, we observed a significant task effect ($F_{(2,530)} = 17.23, p < 0.0001$), with resting state scans showing overall higher functional connectivity compared with the gambling ($p < 0.001$) and thermal pain ($p < 0.01$) tasks. Despite these differences in baseline connectivity, we did not observe any significant task × target interaction ($F_{(18,530)} = 1.39, p = 0.13$) and only a modest subregion × task effect interaction ($F_{(2,530)} = 2.45, p < 0.05$). Similar to the structural connectivity results, we observed large target ($F_{(9,530)} = 23.26, p < 0.0001$) and target × subdivision interaction ($F_{(9,530)} = 35.71, p < 0.0001$) effects. Finally, we observed no significant three-way interaction of target × subdivision × task effect ($F_{(18,530)} = 0.79, p = 0.71$). These results indicate that *p*core and *p*shell have robust differential connectivity patterns to cortical and subcortical structures during different cognitive states and at rest. For all scans, the *p*core showed higher connectivity to the BG, CG, FP, INS, PCG, and TH. In contrast, the *p*shell showed higher connectivity to AMYG, OFC, and SCC. There were no differences in HIP connectivity (Table 2). Thus, functional and anatomical connectivity patterns show similarities, as well as im-

portant differences, yet both fingerprints differentiate between NAc subdivisions.

Left and right NAc subdivisions exhibit similar anatomical and functional connectivity

Here we compare the structural (DTI) and functional connectivity of the left NAc subdivisions to their right counterparts. Left *p*core and *p*shell subdivisions were generated by flipping the spatial coordinates of the right *p*core and *p*shell along the *x*-axis (Fig. 7A). Examining the connectivity of the left NAc subdivisions allows us both to determine differences in left and right NAc connectivity and to validate the spatial contiguity of the right subdivisions using the left (unbiased) connectivity results. The structural and functional fingerprints for the left NAc are shown in Figure 7B. Similar to the right subdivisions, DTI connectivity exhibited significant target effect ($F_{(9,250)} = 37.55$, $p < 0.0001$) and subdivision × target interaction ($F_{(9,250)} = 12.09$, $p < 0.0001$), but a nonsignificant subdivision effect ($F_{(1,250)} = 1.361$, $p = 0.29$). Significant differences in the *p*core and *p*shell connectivity to each target regions were determined using a Tukey-HSD *post hoc* analysis. The left *p*core exhibited higher structural connectivity to the left BG, FP, and OFC. In contrast, the left *p*shell showed higher structural connectivity to AMYG. Similar to the right NAc, left NAc subdivisions showed equivalent connectivity strength to the HIP, INS, PCG, SC, and TH (Tukey-HSD *post hoc* analysis).

Functional connectivity of the left NAc during resting state was also examined using a two-way repeated measure ANOVA (NAc subdivisions and target regions). Functional connectivity showed a significant target ($F_{(1,246)} = 14.19$, $p < 0.0001$), subdivision ($F_{(1,246)} = 12.45$, $p < 0.0001$), and target × subdivision interaction ($F_{(9,246)} = 9.34$, $p < 0.0001$) effect. The left *p*core showed higher functional connectivity to the left BG, INS, PCG, and TH. In contrast, the left *p*shell showed higher connectivity to AMYG, OFC, and SCC. There were no differences in FP and HIP connections. Overall, the left and right NAc subdivisions showed similar functional and structural connectivity patterns. This result corroborates the *p*core and *p*shell spatial and functional segregation across hemispheres.

Discussion

The present study, for the first time, demonstrates that human neuroimaging data can be used to segregate the NAc into two structurally and functionally distinct components that we designate putative core (*p*core) and shell (*p*shell). Using the state-of-the-art, probabilistic tractography methodology (O'Shea et al., 2007; Johansen-Berg and Rushworth, 2009), in every subject, we identify two NAc components of approximately equal volumes albeit with variable borders. It remains unclear whether the across-subject variability is a reflection of actual across-subject anatomical differences or more a reflection of technical limitations of DTI-based probabilistic tractography (Johansen-Berg and Rushworth, 2009). When we compare this spatial pattern with the best quality human postmortem material, we observe an approximate correspondence, although the exact borders of the human NAc and its components remain generally unclear in postmortem tissue (Meredith et al., 1996; Voorn et al., 1996; Morel et al., 2002), and across-subject variability remains unclear given the paucity of such material. It does seem that our rostro-
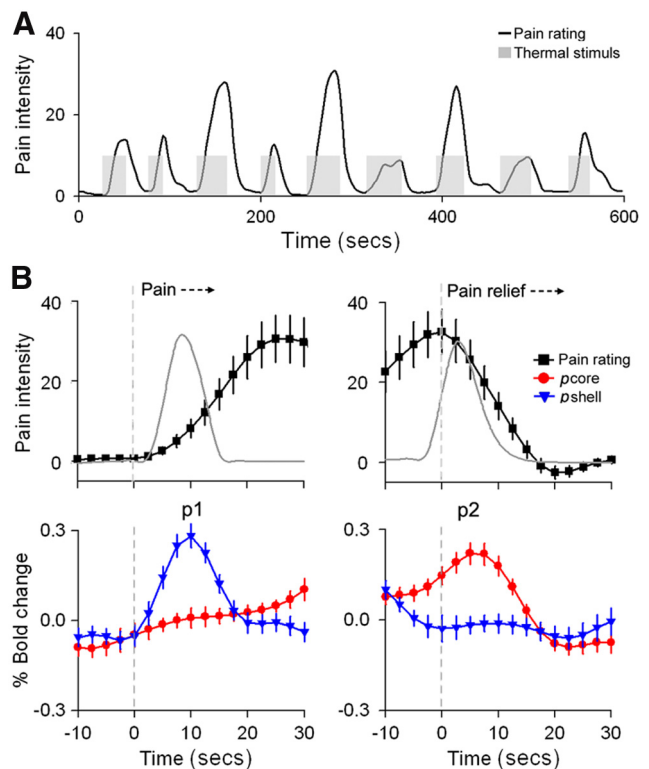

Figure 5. NAc subdivisions show differential activation for onset and offset of acute thermal pain. *A*, The thermal pain task. Average pain ratings (black) and the time course of the painful heat (gray) applied to the skin. Data are from Baliki et al. (2010). *B*, Top panels, Mean ± SEM time course of the pain rating (convolved with hemodynamic function) during start (left) and end (right) of thermal stimulus. The time courses were averaged across all stimulation epochs where subjects reported pain. The gray lines indicate absolute value of the derivative, $|d/dt|$, for the stimulus. Bottom panels, Average BOLD response time course for right NAc, *p*core (red) and *p*shell (blue) for the same time periods. Data are mean ± SEM. Anticipation of impending pain transiently activates the *p*shell (p1), whereas anticipation of pain relief transiently activates the *p*core (p2).
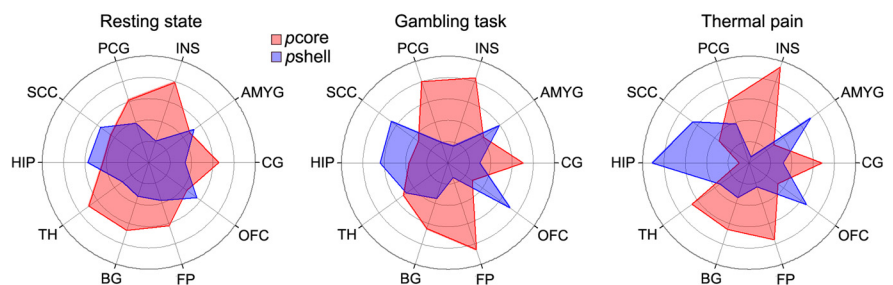

Figure 6. The NAc subdivisions exhibit distinct functional connectivity patterns. Polar plots represent the functional connectivity fingerprints in the right hemisphere for different scans. The values indicate relative functional connection for *p*shell and *p*core of the right NAc to the 10 targets. The NAc subdivisions exhibit similar functional connectivity patterns for resting state, gambling, and thermal pain scans. Target abbreviations are listed in Figure 3.

caudal segregation of human NAc subdivisions is more distinct than the corresponding subregions in rat, marmoset, or macaque (Meredith et al., 1996; Fudge and Haber, 2002; Haber and Knutson, 2010; Haber, 2011). Based on the group-averaged *p*core and *p*shell, we were able to show and validate that these subdivisions demonstrate distinct structural and functional connectivity to prefrontal and limbic targets, as well as differential activation for valuation of reward for hedonically opposite tasks.

The DTI-based structural connectivity showed that *p*core was preferentially connected to BG, FP, OFC, and TH, *p*shell was

Table 2. Functional connectivity differences between the two NAc subdivisions[a]

ROI	Resting state		Gambling		Thermal pain[b]		
	pcore	pshell	pcore	pshell	pcore	pshell	p
AMYG	0.11 ± 0.02	0.12 ± 0.02	0.07 ± 0.02	0.10 ± 0.02	0.05 ± 0.02	0.12 ± 0.02	<0.05
BG	0.21 ± 0.02	0.10 ± 0.01	0.16 ± 0.03	0.08 ± 0.02	0.15 ± 0.02	0.12 ± 0.02	<0.001
CG	0.13 ± 0.02	0.07 ± 0.02	0.05 ± 0.03	0.02 ± 0.03	0.06 ± 0.03	0.03 ± 0.03	<0.001
FP	0.11 ± 0.02	0.07 ± 0.02	0.09 ± 0.02	0.02 ± 0.02	0.06 ± 0.02	0.02 ± 0.02	<0.001
HIP	0.04 ± 0.01	0.06 ± 0.01	0.04 ± 0.02	0.06 ± 0.02	0.01 ± 0.02	0.06 ± 0.03	NS
INS	0.08 ± 0.02	0.02 ± 0.02	0.05 ± 0.03	0.01 ± 0.03	0.05 ± 0.03	0.01 ± 0.03	<0.001
OFC	0.28 ± 0.04	0.37 ± 0.04	0.09 ± 0.05	0.23 ± 0.05	0.13 ± 0.05	0.27 ± 0.05	<0.001
PCG	0.15 ± 0.03	0.09 ± 0.02	0.08 ± 0.03	0.02 ± 0.03	0.09 ± 0.03	0.05 ± 0.03	<0.001
SCC	0.26 ± 0.03	0.33 ± 0.02	0.12 ± 0.04	0.23 ± 0.03	0.16 ± 0.03	0.30 ± 0.03	<0.001
TH	0.12 ± 0.02	0.06 ± 0.02	0.10 ± 0.03	0.08 ± 0.02	0.09 ± 0.02	0.05 ± 0.02	<0.001

[a]Data are mean ± SEM; parametric estimates between seed regions (pcore or pshell) and 10 target regions. Differences in connectivity across tasks (resting state, gambling, and thermal pain) and NAc subdivision (pcore and pshell) and target ROIs were performed using a three-way ANOVA.

[b]Differences in functional connectivity between pcore and pshell to each ROI across all tasks using a post hoc Tukey test.
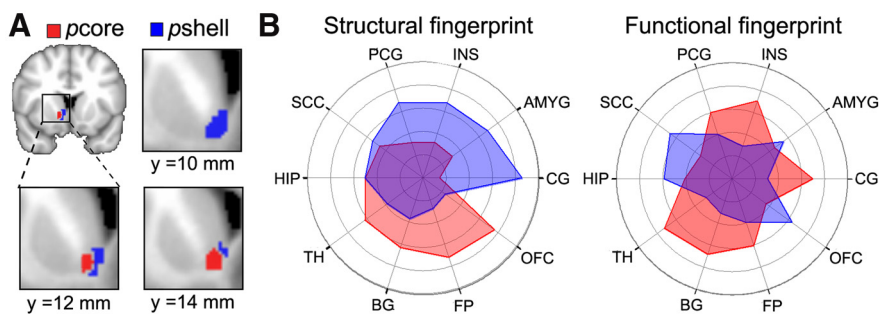
NS, Not significant.

Figure 7. Left and right hemisphere NAc subdivisions exhibit similar, within hemisphere, connectivity properties. **A**, Panels represent the left NAc subdivisions, derived by flipping the coordinates of right NAc subdivisions. **B**, Polar plots represent the structural and resting state functional connectivity fingerprints in the left hemisphere to the subdivisions of left NAc. The values indicate relative structural (left plot) and functional connections (right plot) for pshell and pcore to the 10 targets. Overall, the left NAc subdivisions showed similar structural and functional connectivity to their right counterparts.

more strongly connected to AMYG, whereas for targets CG, HIP, INS, PCG, and SCC structural connections could not be differentiated between pcore and pshell, in the left and right hemispheres. It should first be noted that these seed-to-target structural connections are based primarily on the DTI properties of ventral prefrontal white matter tracks. There is strong validation evidence for the DTI-based connections that we studied for subdivisions of NAc because the prefrontal tracks studied here exhibit close correspondence between macaque tracer-based measurements and diffusion MRI tractography of both macaques and humans (Jbabdi et al., 2013). The preferential structural connectivity of pcore with BG and OFC, and for pshell with AMYG, is consistent with the reported differential inputs and outputs of NAc subdivisions in the rat and the monkey (Meredith et al., 1996; Fudge and Haber, 2002; Haber and Knutson, 2010; Haber, 2011), whereas equipotent connectivity of HIP to both pcore and pshell was unexpected (in the rodent, HIP inputs target primarily the medial shell of NAc) (Britt et al., 2012) and may be peculiar to the human NAc. Yet the precise correspondence between our observed differential structural connectivity for human NAc subdivisions and animal tracer studies remains vague because of multiple technical limitations: (1) DTI-based connectivity cannot distinguish between afferent and efferent projections. (2) It is also not clear the extent to which DTI-based connectivity captures focal and diffuse projections to NAc (Mailly et al., 2013). (3) The targets we examined were derived from standard atlas anatomical divisions that approximate Brodmann areas, and components of these targets may show further

preferential connectivity (e.g., CG at the genu in contrast to posterior CG may exhibit distinct connections to NAc subdivisions). (4) Vagaries regarding rodent and human correspondences of prefrontal subdivisions decrease ability of performing direct comparisons regarding projections to NAc (e.g., rodent projections described in Mailly et al., 2013). There is a complex relationship between structural connectivity and functional connectivity. During resting state conditions, the presence of the former implies the latter (but not the other way round), but this relationship becomes disrupted in active tasks (Honey et al., 2009; Baria et al., 2013). During resting state and in both active tasks, we observe preservation of connectivity for many of the targets to NAc subdivisions. However, OFC shifts to become more strongly linked to pshell, together with HIP and SCC, whereas INS and PCG become more connected to pcore. These connectivity shifts are likely a reflection of shifts in specific regions linked to NAc subdivisions within the large targets studied, as well as the complex interplay between focal and diffuse prefrontal and limbic inputs (Mailly et al., 2013), and dopaminergic modulation. More importantly, across three task conditions and despite the shifts in connectivity patterns, we continue to observe specificity of functional connectivity for NAc subdivisions.

Additionally, we could demonstrate that valuation for two hedonically opposing tasks (monetary gambles and pain) are represented differentially in the two subdivisions of NAc. Findings that positive and negative effects co-occur in emotionally charged situations (Miller, 1959; Berridge and Grill, 1984; Schimmack, 2001; Larsen et al., 2004) already hint at separate brain representations of positive and negative value (Cacioppo, 1994). Neuroimaging studies consistently implicate NAc in monetary gains or losses, anticipation of immediate outcomes, experience of gains or losses, or for potential gains or losses when a decision is being made (Breiter et al., 2001; O'Doherty et al., 2003; Tricomi et al., 2004; Zink et al., 2004; Tobler et al., 2007; Tom et al., 2007). Monetary losses and gains are shown to be processed by a unitary (appetitive) system, centered in the NAc (with increased BOLD for gains and decreased BOLD for losses) (Tom et al., 2007). However, there is also evidence that gains and losses are repre-

sented (with increased BOLD for both) in different portions of the striatum (Seymour et al., 2007). Additionally, when actions lead concurrently to the delivery of both money and pain, the related reward-predictive signal coactivates parts of the dorsal striatum (an integrated response) (Seymour et al., 2012). Our results are more consistent with Tom et al. (2007) and indicate that specifically the *p*shell part of the NAc reflects unitary appetitive response to monetary gambles, whereas *p*core is activated independent of perceived gains or losses.

As for the thermal pain task, we observe the opposite pattern, namely, anticipation of value of cessation of pain (analgesia) specifically activated *p*core portion of NAc. These results extend recent evidence in rodents showing that reward value of pain relief increases dopamine release in NAc and activates ventral tegmental dopaminergic cells (Navratilova et al., 2012). In addition, we see that anticipation of impending pain engages *p*shell of NAc. A recent rodent study demonstrates that a fear cue also results in increased transmission in the NAc shell but decreased dopamine transmission within the NAc core (Badrinarayan et al., 2012). Assuming that the NAc activity we observe in humans is mainly a reflection of dopaminergic activity, then our results and the rodent evidence together suggest the generalization that anticipation of aversive events involves enhanced dopaminergic activity in shell but not the core in both species. Recent evidence indicates that inactivation of D2 receptors, in the indirect striatopallidal pathway in rodents, is necessary for both acquisition and expression of aversive behavior, and direct pathway D1 receptor activation controls reward-based learning (Hikida et al., 2010; Hikida et al., 2013). It seems we can conclude that direct and indirect pathways of the NAc, via D1 and D2 receptors, subserve distinct anticipation and valuation roles in the shell and core of NAc, which is consistent with observations regarding spatial segregation and diversity of responses of midbrain dopaminergic neurons for rewarding and aversive conditions, some encoding motivational value, others motivational salience, each connected with distinct brain networks and having distinct roles in motivational control (Bromberg-Martin et al., 2010; Cohen et al., 2012; Lammel et al., 2013).

Overall, we show that the human accumbens can be subdivided into two distinct subdivisions, *p*shell and *p*core, each exhibiting preferential structural and functional connectivity, and encoding value for positive rewards and for pain relief, respectively. The structural and functional connectivity for the two subdivisions in the human show deviations from that described in rodents, yet technical and anatomical differences obviate direct comparisons. The spatial distinctions for activity predicting monetary reward and for pain relief seem to have closer correspondences to recent evidence in rodents regarding segregation of NAc pathways regarding reward and aversive behavior. Importantly, the present results show that the pain system is an integral component of the mesocorticolimbic circuitry; as such, perceptual and behavioral outputs resulting from nociceptive activity (i.e., pain) must be considered part of the driving force for the organism's appropriate response to environmental cues (the price people pay for relief of pain is strongly determined by the local context of the market) (Vlaev et al., 2009), and motor execution is influenced by relative pain differences between choices (Kurniawan et al., 2010). Thus, pain perception and related behavior must be shaped and modulated by motivational learning circuitry (Apkarian, 2008; Flor, 2012), probably through the indirect D2 pathway. Yet pain and reward mesocorticolimbic circuits are also interactive (Seymour et al., 2012), as recent evidence shows that, when monetary reward decisions are made in the presence of pain, the NAc reward predictive signal becomes attenuated (Talmi et al., 2009).

References

Alexander GE, DeLong MR, Strick PL (1986) Parallel organization of functionally segregated circuits linking basal ganglia and cortex. Annu Rev Neurosci 9:357–381. CrossRef Medline

Ambroggi F, Ishikawa A, Fields HL, Nicola SM (2008) Basolateral amygdala neurons facilitate reward-seeking behavior by exciting nucleus accumbens neurons. Neuron 59:648–661. CrossRef Medline

Apkarian AV (2008) Pain perception in relation to emotional learning. Curr Opin Neurobiol 18:464–468. CrossRef Medline

Badrinarayan A, Wescott SA, Vander Weele CM, Saunders BT, Couturier BE, Maren S, Aragona BJ (2012) Aversive stimuli differentially modulate real-time dopamine transmission dynamics within the nucleus accumbens core and shell. J Neurosci 32:15779–15790. CrossRef Medline

Baldo BA, Kelley AE (2007) Discrete neurochemical coding of distinguishable motivational processes: insights from nucleus accumbens control of feeding. Psychopharmacology 191:439–459. CrossRef Medline

Baliki MN, Geha PY, Fields HL, Apkarian AV (2010) Predicting value of pain and analgesia: nucleus accumbens response to noxious stimuli changes in the presence of chronic pain. Neuron 66:149–160. CrossRef Medline

Baria AT, Mansour A, Huang L, Baliki MN, Cecchi GA, Mesulam MM, Apkarian AV (2013) Linking human brain local activity fluctuations to structural and functional network architectures. Neuroimage 73:144–155. CrossRef Medline

Basar K, Sesia T, Groenewegen H, Steinbusch HW, Visser-Vandewalle V, Temel Y (2010) Nucleus accumbens and impulsivity. Prog Neurobiol 92:533–557. CrossRef Medline

Bassareo V, De Luca MA, Di Chiara G (2002) Differential expression of motivational stimulus properties by dopamine in nucleus accumbens shell versus core and prefrontal cortex. J Neurosci 22:4709–4719. Medline

Becerra L, Borsook D (2008) Signal valence in the nucleus accumbens to pain onset and offset. Eur J Pain 12:866–869. CrossRef Medline

Becerra L, Breiter HC, Wise R, Gonzalez RG, Borsook D (2001) Reward circuitry activation by noxious thermal stimuli. Neuron 32:927–946. CrossRef Medline

Berridge KC, Grill HJ (1984) Isohedonic tastes support a two-dimensional hypothesis of palatability. Appetite 5:221–231. CrossRef Medline

Breiter HC, Aharon I, Kahneman D, Dale A, Shizgal P (2001) Functional imaging of neural responses to expectancy and experience of monetary gains and losses. Neuron 30:619–639. CrossRef Medline

Brischoux F, Chakraborty S, Brierley DI, Ungless MA (2009) Phasic excitation of dopamine neurons in ventral VTA by noxious stimuli. Proc Natl Acad Sci U S A 106:4894–4899. CrossRef Medline

Britt JP, Benaliouad F, McDevitt RA, Stuber GD, Wise RA, Bonci A (2012) Synaptic and behavioral profile of multiple glutamatergic inputs to the nucleus accumbens. Neuron 76:790–803. CrossRef Medline

Bromberg-Martin ES, Matsumoto M, Hikosaka O (2010) Dopamine in motivational control: rewarding, aversive, and alerting. Neuron 68:815–834. CrossRef Medline

Cacioppo JTB (1994) Relationship between attitudes and evaluative space: a critical review, with emphasis on the separability of positive and negative substrates. Psychol Bull 115:401–423. CrossRef

Cohen JY, Haesler S, Vong L, Lowell BB, Uchida N (2012) Neuron-type-specific signals for reward and punishment in the ventral tegmental area. Nature 482:85–88. CrossRef Medline

Fields HL, Hjelmstad GO, Margolis EB, Nicola SM (2007) Ventral tegmental area neurons in learned appetitive behavior and positive reinforcement. Annu Rev Neurosci 30:289–316. CrossRef Medline

Flor H (2012) New developments in the understanding and management of persistent pain. Curr Opin Psychiatry 25:109–113. CrossRef Medline

Fudge JL, Haber SN (2002) Defining the caudal ventral striatum in primates: cellular and histochemical features. J Neurosci 22:10078–10082. Medline

Haber SN (2011) Neuroanatomy of reward: a view from the ventral striatum. In: Neurobiology of sensation and reward (Gottfried JA, ed). Boca Raton, FL: CRC.

Haber SN, Knutson B (2010) The reward circuit: linking primate anatomy

and human imaging. Neuropsychopharmacology 35:4–26. CrossRef Medline

Hikida T, Kimura K, Wada N, Funabiki K, Nakanishi S (2010) Distinct roles of synaptic transmission in direct and indirect striatal pathways to reward and aversive behavior. Neuron 66:896–907. CrossRef Medline

Hikida T, Yawata S, Yamaguchi T, Danjo T, Sasaoka T, Wang Y, Nakanishi S (2013) Pathway-specific modulation of nucleus accumbens in reward and aversive behavior via selective transmitter receptors. Proc Natl Acad Sci U S A 110:342–347. CrossRef Medline

Honey CJ, Sporns O, Cammoun L, Gigandet X, Thiran JP, Meuli R, Hagmann P (2009) Predicting human resting-state functional connectivity from structural connectivity. Proc Natl Acad Sci U S A 106:2035–2040. CrossRef Medline

Jbabdi S, Lehman JF, Haber SN, Behrens TE (2013) Human and monkey ventral prefrontal fibers use the same organizational principles to reach their targets: tracing versus tractography. J Neurosci 33:3190–3201. CrossRef Medline

Johansen-Berg H, Rushworth MF (2009) Using diffusion imaging to study human connectional anatomy. Annu Rev Neurosci 32:75–94. CrossRef Medline

Joshua M, Adler A, Mitelman R, Vaadia E, Bergman H (2008) Midbrain dopaminergic neurons and striatal cholinergic interneurons encode the difference between reward and aversive events at different epochs of probabilistic classical conditioning trials. J Neurosci 28:11673–11684. CrossRef Medline

Kurniawan IT, Seymour B, Vlaev I, Trommershäuser J, Dolan RJ, Chater N (2010) Pain relativity in motor control. Psychol Sci 21:840–847. CrossRef Medline

Lammel S, Lim BK, Malenka RC (2013) Reward and aversion in a heterogeneous midbrain dopamine system. Neuropharmacology. Advance online publication. Retrieved April 8, 2013. doi: 10.1016/j.neuropharm.2013.03.019. CrossRef

Larsen JT, McGraw AP, Mellers BA, Cacioppo JT (2004) The agony of victory and thrill of defeat: mixed emotional reactions to disappointing wins and relieving losses. Psychol Sci 15:325–330. CrossRef Medline

Lüscher C, Malenka RC (2011) Drug-evoked synaptic plasticity in addiction: from molecular changes to circuit remodeling. Neuron 69:650–663. CrossRef Medline

Mailly P, Aliane V, Groenewegen HJ, Haber SN, Deniau JM (2013) The rat prefrontostriatal system analyzed in 3D: evidence for multiple interacting functional units. J Neurosci 33:5718–5727. CrossRef Medline

Meredith GE, Pattiselanno A, Groenewegen HJ, Haber SN (1996) Shell and core in monkey and human nucleus accumbens identified with antibodies to calbindin-D28k. J Comp Neurol 365:628–639. CrossRef Medline

Miller NE (1959) Liberalization of basic SR concepts: extensions to conflict behavior motivation and social learning. In: Psychology: a study of a science (Koch S, ed), pp 196–292. New York: McGraw-Hill.

Mirenowicz J, Schultz W (1996) Preferential activation of midbrain dopamine neurons by appetitive rather than aversive stimuli. Nature 379:449–451. CrossRef Medline

Montague PR, Berns GS (2002) Neural economics and the biological substrates of valuation. Neuron 36:265–284. CrossRef Medline

Montague PR, King-Casas B, Cohen JD (2006) Imaging valuation models in human choice. Annu Rev Neurosci 29:417–448. CrossRef Medline

Morel A, Loup F, Magnin M, Jeanmonod D (2002) Neurochemical organization of the human basal ganglia: anatomofunctional territories defined by the distributions of calcium-binding proteins and SMI-32. J Comp Neurol 443:86–103. CrossRef Medline

Navratilova E, Xie JY, Okun A, Qu C, Eyde N, Ci S, Ossipov MH, King T, Fields HL, Porreca F (2012) Pain relief produces negative reinforcement through activation of mesolimbic reward-valuation circuitry. Proc Natl Acad Sci U S A 109:20709–20713. CrossRef Medline

O'Doherty JP (2004) Reward representations and reward-related learning in the human brain: insights from neuroimaging. Curr Opin Neurobiol 14:769–776. CrossRef Medline

O'Doherty JP, Dayan P, Friston K, Critchley H, Dolan RJ (2003) Temporal difference models and reward-related learning in the human brain. Neuron 38:329–337. CrossRef Medline

O'Shea J, Sebastian C, Boorman ED, Johansen-Berg H, Rushworth MF (2007) Functional specificity of human premotor-motor cortical interactions during action selection. Eur J Neurosci 26:2085–2095. CrossRef Medline

Platt ML, Huettel SA (2008) Risky business: the neuroeconomics of decision making under uncertainty. Nat Neurosci 11:398–403. CrossRef Medline

Roitman MF, Wheeler RA, Wightman RM, Carelli RM (2008) Real-time chemical responses in the nucleus accumbens differentiate rewarding and aversive stimuli. Nat Neurosci 11:1376–1377. CrossRef Medline

Schimmack U (2001) Pleasure, displeasure, and mixed feelings: are semantic opposites mutually exclusive? Cogn Emotion 15:81–97. CrossRef

Schultz W, Dayan P, Montague PR (1997) A neural substrate of prediction and reward. Science 275:1593–1599. CrossRef Medline

Scott DJ, Heitzeg MM, Koeppe RA, Stohler CS, Zubieta JK (2006) Variations in the human pain stress experience mediated by ventral and dorsal basal ganglia dopamine activity. J Neurosci 26:10789–10795. CrossRef Medline

Seymour B, O'Doherty JP, Koltzenburg M, Wiech K, Frackowiak R, Friston K, Dolan R (2005) Opponent appetitive-aversive neural processes underlie predictive learning of pain relief. Nat Neurosci 8:1234–1240. CrossRef Medline

Seymour B, Daw N, Dayan P, Singer T, Dolan R (2007) Differential encoding of losses and gains in the human striatum. J Neurosci 27:4826–4831. CrossRef Medline

Seymour B, Daw ND, Roiser JP, Dayan P, Dolan R (2012) Serotonin selectively modulates reward value in human decision-making. J Neurosci 32:5833–5842. CrossRef Medline

Smith KS, Berridge KC, Aldridge JW (2011) Disentangling pleasure from incentive salience and learning signals in brain reward circuitry. Proc Natl Acad Sci U S A 108:E255–E264. CrossRef Medline

Talmi D, Dayan P, Kiebel SJ, Frith CD, Dolan RJ (2009) How humans integrate the prospects of pain and reward during choice. J Neurosci 29:14617–14626. CrossRef Medline

Thompson RH, Swanson LW (2010) Hypothesis-driven structural connectivity analysis supports network over hierarchical model of brain architecture. Proc Natl Acad Sci U S A 107:15235–15239. CrossRef Medline

Tobler PN, O'Doherty JP, Dolan RJ, Schultz W (2007) Reward value coding distinct from risk attitude-related uncertainty coding in human reward systems. J Neurophysiol 97:1621–1632. CrossRef Medline

Tom SM, Fox CR, Trepel C, Poldrack RA (2007) The neural basis of loss aversion in decision-making under risk. Science 315:515–518. CrossRef Medline

Tomassini V, Jbabdi S, Klein JC, Behrens TE, Pozzilli C, Matthews PM, Rushworth MF, Johansen-Berg H (2007) Diffusion-weighted imaging tractography-based parcellation of the human lateral premotor cortex identifies dorsal and ventral subregions with anatomical and functional specializations. J Neurosci 27:10259–10269. CrossRef Medline

Tricomi EM, Delgado MR, Fiez JA (2004) Modulation of caudate activity by action contingency. Neuron 41:281–292. CrossRef Medline

Vlaev I, Seymour B, Dolan RJ, Chater N (2009) The price of pain and the value of suffering. Psychol Sci 20:309–317. CrossRef Medline

Voorn P, Brady LS, Berendse HW, Richfield EK (1996) Densitometrical analysis of opioid receptor ligand binding in the human striatum: I. Distribution of μ opioid receptor defines shell and core of the ventral striatum. Neuroscience 75:777–792. CrossRef Medline

Wanigasekera V, Lee MC, Rogers R, Kong Y, Leknes S, Andersson J, Tracey I (2012) Baseline reward circuitry activity and trait reward responsiveness predict expression of opioid analgesia in healthy subjects. Proc Natl Acad Sci U S A 109:17705–17710. CrossRef Medline

Zahm DS (2000) An integrative neuroanatomical perspective on some subcortical substrates of adaptive responding with emphasis on the nucleus accumbens. Neurosci Biobehav Rev 24:85–105. CrossRef Medline

Zahm DS, Brog JS (1992) On the significance of subterritories in the "accumbens" part of the rat ventral striatum. Neuroscience 50:751–767. CrossRef Medline

Zink CF, Pagnoni G, Martin-Skurski ME, Chappelow JC, Berns GS (2004) Human striatal responses to monetary reward depend on saliency. Neuron 42:509–517. CrossRef Medline